#### **ORIGINAL ARTICLE**





# Hemodynamic Characterization of Peripheral Arterio-Venous Malformations Using Rapid Contrast-Enhanced MR Imaging: An In Vitro and In Vivo Study

Camilla Giulia Calastra 

· Marika Bono · Aloma Blanch Granada · Aleksandra Tuleja 

· Sarah Maike Bernhard · Vanessa Diaz-Zuccarini · Stavroula Balabani · Dominik Obrist 

· Hendrik von Tengg-Kobligk · Bernd Jung · Ernd · Ernd

Received: 17 February 2025 / Accepted: 19 May 2025 / Published online: 13 June 2025 © The Author(s) 2025

#### **Abstract**

**Purpose** Peripheral arterio-venous malformations (pAVMs) are vascular defects often requiring extensive medical treatment. To improve disease management, hemodynamic markers based on 2D Digital Subtraction Angiography (DSA) data were previously defined to classify pAVMs. However, DSA offers only 2D information, involves ionizing radiation, and requires intra-arterial intervention. We hypothesized that pAVMs could be classified with the same approach with 3D dynamic contrast-enhanced MR-based data. To this end, the present work aims to develop a computational classification system for pAVMs using 3D dynamic contrast-enhanced MR-based data.

**Methods** A pAVM phantom was imaged using both DSA and MRI to validate the methodology, which was then applied to 10 MR-based in vivo datasets. A semi-automated vessel detection algorithm, based on the standard deviation of each voxel or pixel in time, was used. Classification was performed by identifying the time of arrival (CA<sub>ToA</sub>) of contrast agent (CA) and the maximum time derivative of the CA transport in each pixel or voxel (CA<sub>si</sub>).

**Results** Normalized  $CA_{ToA}$  and  $CA_{si}$  histograms showed no significant difference between in vitro DSA and MRI (respectively  $\chi^2 = 0.20$ , p = 0.65 and  $\chi^2 = 0.21$ , p = 0.65), validating the methodology to classify pAVMs.  $CA_{ToA}$  histograms for type II–IV AVMs derived from in vivo MR-based data aligned with DSA patterns and known hemodynamics.  $CA_{ToA}$  histograms of capillary–venulous AVMs were distinct, with non-zero values at later times than other AVM types, representing late venous drainage. Type IV AVMs histograms for  $CA_{si}$  were more right-skewed than those derived from types II and III pAVMs.

**Conclusions** MR image quality and temporal resolution are sufficient to allow a classification of pAVMs. This classification method has the potential to become a diagnostic tool for the surgical navigation of pAVMs for clinicians.

Keywords Vascular malformations · Yakes AVMs classification · MR imaging · Validation · CE-trMRA

| st |
|----|
|    |
|    |
| c  |
|    |
|    |
|    |
|    |
|    |
|    |
|    |
|    |
|    |
|    |
|    |
| •  |



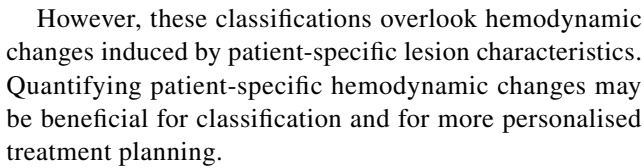
ToA Time of arrival US Ultrasound V Volume

# Introduction

Congenital vascular malformations (CVMs) are localized anomalies arising during the embryonic development of the vascular system [1]. CVMs can occur anywhere in the body and exhibit varying blood flow dynamics. Peripheral arteriovenous malformations (pAVMs), a CVM subtype, are high-flow congenital defects found outside the central nervous system [2] and have a prevalence of approximately 0.03% [3]. pAVMs consist of tangles of abnormal blood vessels where the feeding arteries are directly connected to a venous drainage network, without the interposition of capillaries [3]. These malformations tend to become large and complex, leading to various physical complications including tissue damage due to the steal phenomenon and consecutive ischemia, venous hypertension, excessive tissue growth, and volume overload of the heart.

The gold standard imaging technique for diagnosing and treating pAVMs is dynamic intra-arterial catheter-based 2D digital subtraction angiography, DSA [4, 5], a mere luminography, often supplemented by magnetic resonance (MR) imaging and duplex ultrasound (US). MR Imaging plays a role in the first-time diagnosis [6] by offering a non-invasive imaging modality which delineates the nidus, feeding arteries, and draining veins. It is also used in the planning of the surgical treatment for the 3D localization of the pAVM and for post-therapy follow-up, providing a radiation-free alternative to repeated DSA, especially valuable in younger or recurrent patients [7].

Extensive treatment may be required for pAVMs due to their impact on local tissue structures and the cardiovascular system [8], involving repeated exposure to X-ray radiation and surgical interventions. Additionally, the intricate structure and altered blood flow patterns of pAVMs often make treatment challenging and sometimes unsuccessful [9]. Several classification systems, including that of Yakes et al. [8, 9], have been developed to guide pAVMs treatment based on standardized lesion angioarchitectures. Yakes classification categorizes pAVMs in type I, a direct artery-to-vein shunt; type II, multiple arteries connected to vein-venular structures (nidus); type III, multiple arteries lead to a single aneurysmal vein (type IIIa) or multiple dilated veins (type IIIb); and type IV, microfistulous connections with parallel capillary perfusion. In addition, recently, a new subgroup of microfistular pAVMs, the capillary-venulous arterio-venous (CV-AVM) has been proposed, composed of fistulous paths on the venous half of capillaries and dilated draining venules [10, 11].



So far, medical image processing techniques integrated with engineering tools have shown promise for predicting vascular hemodynamics [12–14], leading to the identification of hemodynamic biomarkers in several vascular diseases, including aortic dissection [15–18], coronary artery disease [19], peripheral arterial disease [20], and cerebral aneurysms [21]. Studies have investigated hemodynamic patterns and treatment strategies through computational modeling [22–24] and treatment outcomes with the use of machine learning [25, 26] for cerebral AVMs (cAVMs). Even if medical imaging processing with machine learning is increasingly applied to vascular problems, we are not aware of such studies in the context of pAVMs.

Recently, Frey et al. [27] used the information on the transport of contrast agent (CA) as captured by dynamic DSA to define markers to characterize and classify pAVMs by their distinct hemodynamic appearance.

To further validate and develop such hemodynamic markers, artificial vascular models offer a powerful platform for investigating patient-specific flow dynamics under controlled conditions.

These models have been extensively used in cardio-vascular research for exploring blood flow mechanics [28–30], pre-surgical planning [31–33], and validating imaging techniques [33–35].

However, due to the structural complexity and small vessel dimensions of pAVMs, their application in this context is still in its early stages. Recent works have demonstrated the feasibility of constructing physiologically realistic 3D-printed models of both cAVMs [35] and pAVMs [30, 36], enabling flow characterization in vitro.

We hypothesize that state-of-the-art MR Imaging acceleration techniques, such as Parallel Imaging [37–42] and Compressed Sensing [43–46], in combination with image processing may enable the classification of pAVMs using the hemodynamic markers described in [27].

To this end, the present work aims to develop a computational classification system for pAVMs using non-invasive, ionizing radiation-free MR Imaging. To achieve this goal, the study is divided into two main parts:

- Validation of the hemodynamic markers in a controlled in vitro experimental set-up in DSA and MR environments
- Application of the image processing algorithm to in vivo MR Imaging datasets.



#### **Materials and Methods**

#### In Vitro Data

To verify the ability of MR Imaging to reproduce the hemodynamic markers originally defined in DSA [27], a direct comparison was conducted between the two modalities with the same phantom under two separate experimental conditions adapted to the respective imaging modalities.

A rigid replica of a type III neck pAVM from a 47-yearold man was fabricated using clear resin via stereolithography, achieving a maximum resolution of 25 µm with a Formlabs Form 3 SLA 3D printer (Formlabs, USA) [36] (Fig. 1a). The patient-specific geometry of the pAVM was segmented from a CT scan as described by Franzetti et al [30]. The reconstructed geometry preserved the spatial configuration of the vascular network, comprising a 3.8 mm diameter feeding artery, a 2 mm arterial outflow, a nidus measuring approximately  $16 \times 12 \times 9$  mm, and two draining veins with diameters of 1.6 mm and 2.3 mm, respectively. The nidus region was modeled as an idealized porous lattice that induces the same pressure drop as the in vivo case, as estimated from the computational fluid dynamic studies of the same pAVM [30]. To facilitate integration with the experimental set-up, minimize flow transitions, and prevent leakages, barbed fittings were added to the inlet and outlets [35].

The dataset was acquired as part of an ethical protocol, and data were used after appropriate patient consent (NHS Health Research 94 Authority, ref: 19/SC/0090). The phantom can be compared to an extremity as one artery has been identified as the main feeder and two veins as the

main draining veins, which resembles the configuration of a pAVM of a foot or a hand, characterized by one of few feeding arteries and one or few draining veins.

The phantom was connected to an experimental setup, with a 90:10 water-glycerol mixture (99%, SIGALD, Sigma-Aldrich Chemie GmbH, Buchs) used as the working fluid. The resulting density and viscosity of the fluid were  $\rho = 1024.2 \text{ kg/m}^3$  and  $\mu = 1.2744 \text{ mPa}$  s. Although this mixture did not match the viscosity and density of blood, it was selected to match the T1 relaxation time of blood at 3 T [47]. To ensure comparability between imaging modalities, the same working fluid was also used for DSA experiments.

A MR-compatible piston pump (CompuFlow 1000 MR, Shelley Medical Imaging Technologies, Simutec, Ontario, Canada) delivered a patient-specific flow curve. The average inlet flow rate was estimated using patient-specific in vivo DSA data, and a common carotid artery waveform [48] was scaled to match this average flow rate, serving as the inlet boundary condition. Under these conditions, the flow remains laminar and is representative of the blood flow in the studied vasculature. A summary of the experimental parameters for DSA and MR Imaging is reported in Table 1.

In the interventional suite, tubes between the flow pump and the phantom were approximately 1 m long; in the MR scanner suite, tubes were approximately 5 m long to maintain the safety distance between pump unit and scanner. Similarly, the CA injection for DSA was performed approximately 50 cm away from the AVM phantom, whereas in the MR suite approximately 3 m away to mimic clinical practice. The amount of volume injected was chosen to match the in vivo conditions. For MR Imaging, the CA dosage was determined to be 10% (mL) of the patient's body weight (kg) (assumed 80 kg), with a fixed flow rate of Q = 4 mL/s, as for

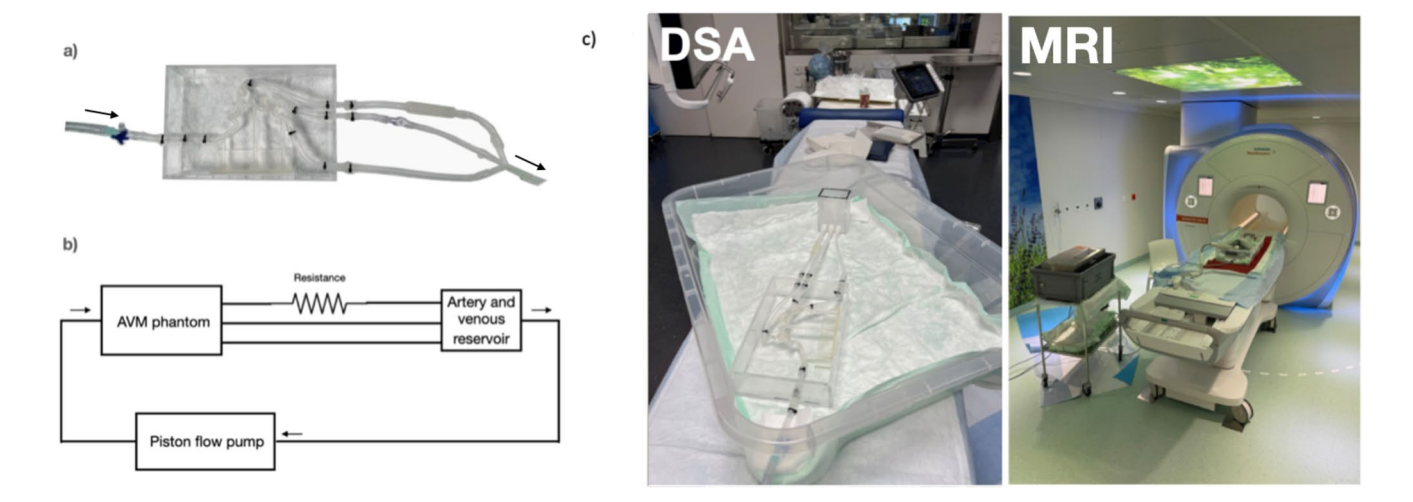


Fig. 1 a 3D-printed pAVM phantom. b Diagram of the experimental set-up. The arrow represents the direction of flow. c Experimental set-up in interventional suite and MR environment



Table 1 Summary of experimental parameters for DSA and MR GRASP

| Parameter                                  | DSA  | GRASP  |
|--|--|--|
| Flow waveform frequency (Hz)               | 1.095  | 0.36   |
| Average flow rate, $Q_{\text{avg}}$ (mL/s) | 1.06   | 0.33   |
| Maximum flow rate, $Q_{\text{max}}$ (mL/s) | 4.82   | 1.59   |
| Average Reynolds number                    | 289.65   | 90.91  |
| Womersley number $(\alpha)$                | 3.49   | 1.87   |
| Injection distance to phantom (m)          | ~0.5   | ~3   |
| Contrast agent (CA)                        | 100% Iodine CA (300 mg/ml, Bracco Suisse SA, Switzerland, Cadempino) | Gadolinium-based CA (GBCA)<br>(Gadovist 1.0 M, Bayer, Switzerland<br>AG, Zurich) |
| CA injection rate (mL/s)                   | 5  | 4  |
| CA injection duration (s)                  | 4  | 2  |
| CA injection volume (mL)                   | 20   | 8  |
| Tubing length (pump to phantom)            | ~ 1.0 m  | ~5.0 m   |

Table 2 Acquisition parameters for in vitro DSA and MR GRASP sequence

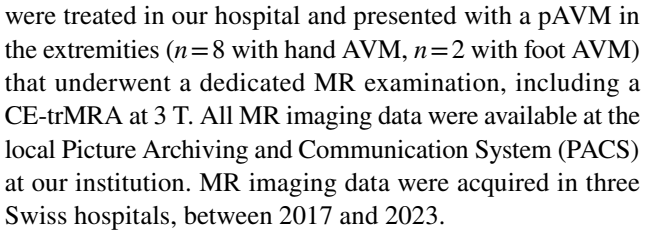
| Parameter                              | DSA                | GRASP              |  |
|--|--------------------|--------------------|--|
| Slice thickness (mm)                   | N/A                | 1.4                |  |
| Temporal resolution (s)                | 0.125              | 1.1                |  |
| $T_{\rm R}$ (ms)                       | N/A                | 3.62               |  |
| $T_{\rm E}$ (ms)                       | N/A                | 1.39               |  |
| Flip angle (°)                         | N/A                | 25                 |  |
| Scan duration (s)                      | 16.125             | 141                |  |
| Spatial resolution (mm)                | $0.15 \times 0.15$ | $1.35 \times 1.35$ |  |
| Field of view (FOV) (mm <sup>2</sup> ) | N/A                | $259 \times 259$   |  |
| Number of projections/slices           | 1                  | 32                 |  |
| Matrix size                            | 1016×1016          | $192 \times 192$   |  |

a clinical in-house protocol. A summary of the CAs used and injection parameters is found in Table 1.

Dynamic DSA was performed using a clinical standard angio suite (Azurion, Philips, Einthoven, NL). 3D contrastenhanced time-resolved magnetic resonance angiography (CE-trMRA) was performed on a clinical 3 T MR scanner (Magnetom Vida, Siemens, Erlangen, Germany) using a Golden-Angle Radial Sparse Parallel (GRASP) sequence. A diagram of the experimental set-up is shown in Fig. 1b, and images of the DSA and MR Imaging setups are provided in Fig. 1c. The acquisition parameters are summarized in Table 2. A receiver 4-element flexible coil was positioned on top of the phantom to be combined with and a 34-element spine coil within the patient MR table.

# In Vivo Data

In this study, 10 CE-trMRA datasets of human in vivo AVMs were analyzed. The cohort comprises patients who



The study received approval from the Ethics Committee of the Canton of Bern (IRB Number 2017-01960) and all patients gave their written informed consent prior to the MR Imaging examination.

By concentrating solely on the extremities, it was possible to make direct lesion comparisons between patients. Details on patients' demographics and image acquisition parameters are found in Table 3.

# **Image-Processing**

#### Preprocessing

The DSA images were first processed using background subtraction; this was done by removing the initial time frame, taken before CA injection, from all subsequent frames. Subsequently both DSA and MR Imaging datasets were organized into a 3D structure for DSA and a 4D structure for CE-trMRA.

Images were cropped to remove irrelevant pixels, artifacts, and overlaid digits. A 1D median filter was used to smooth temporal intensity spikes: a five-time-step window for CE-trMRA and three-time-step for DSA were employed, reflecting differences in spike intensity. A 2D median filter reduced salt and pepper noise. In CE-trMRA, a  $2\times2$  voxel filter was used, which was smaller due to lower spatial resolution compared to  $6\times6$  pixel filter of DSA. Normalization was carried out across all images within the 3D or 4D



**Table 3** pAVM types in hand and foot

| ID    | Туре   | Body region | Temp res. (s) | Sp. res. (mm)        | Sl. thick-<br>ness (mm) | Acquisition scheme |
|-------|--------|-------------|---------------|----------------------|-------------------------|--------------------|
| ID001 | II     | Hand        | 1.100         | $0.741 \times 0.741$ | 2.600                   | Cartesian          |
| ID002 | II     | Hand        | 1.100         | $0.740 \times 0.740$ | 2.600                   | Cartesian          |
| ID003 | II     | Hand        | 4.900         | $1.086 \times 0.717$ | 1.100                   | Cartesian          |
| ID004 | IIIB   | Hand        | 1.300         | $0.741 \times 0.741$ | 2.000                   | Radial             |
| ID005 | IIIB   | Hand        | 4.500         | $0.920 \times 1.395$ | 1.100                   | Cartesian          |
| ID006 | IV     | Foot        | 1.400         | $0.741 \times 0.741$ | 2.000                   | Cartesian          |
| ID008 | CV-AVM | Foot        | 4.600         | $0.741 \times 0.741$ | 2.000                   | Cartesian          |
| ID009 | CV-AVM | Hand        | 1.400         | $0.741 \times 0.741$ | 2.000                   | Cartesian          |
| ID012 | CV-AVM | Hand        | 3.300         | $0.741 \times 0.741$ | 2.600                   | Cartesian          |
| ID020 | IV     | Hand        | 1.300         | $0.741 \times 0.741$ | 2.500                   | Radial             |

*Type* refers to the pAVM type according to Yakes classification, *Temp. res.* temporal resolution, *Sp. res.* spatial resolution, *Sl. thickness* thickness in the *z*-direction, perpendicular to the imaging acquisition plane. Acquisition scheme refers to the acquisition scheme, Cartesian or Radial

intensity volume. A 7–10% noise threshold was applied to balance noise reduction and vessel visualization.

In MR Imaging, a masking procedure was applied by integrating a vessel detection algorithm, which evaluated the standard deviation of intensity values across all voxels over time. A patient-specific standard deviation threshold visually determined and ranging between 2.7 and 3.4, identified voxels exhibiting substantial intensity fluctuations indicative of CA presence.

#### **Postprocessing**

The hemodynamic markers defined by Frey et al. [27] classify pAVMs based on the information derived from the transport of CA as observed in DSA images.

Time of Arrival of the Contrast Agent the time of arrival (ToA) of the CA, denoted as  $CA_{ToA}$ , is calculated as the time from injection until the signal intensity reaches 10% of the maximum signal intensity value. This estimation accounts for different CA arrival times due to the variability of datasets.

CA<sub>ToA</sub> reflects how quickly different vascular territories are reached by the CA. From a clinical perspective, early arrival of CA in the venous system may indicate direct arterio-venous shunting—a hallmark of type I AVMs—whereas delayed and more distributed CA arrival is more typical for complex lesions such as type III AVMs or CV-AVM. These features may have diagnostic value, as shorter CA<sub>ToA</sub> in draining veins reflects faster transit times through low-resistance shunts and may be linked to high-flow lesion.

The  $CA_{TOA}$  values estimated from the in vitro CA distributions were normalized by identifying the pixel or voxel with the longest CA arrival and subtracting each voxel or pixel's  $CA_{TOA}$  from this value, and scaling it by the total effective time in which the CA was present,

obtaining  $CA_{ToA}^{\quad norm}$ . This process accounts for variations in CA injection timing between MR Imaging and DSA and facilitates direct comparisons.

Dispersive Slope of the Contrast Agent the rate of CA increase is determined by calculating the maximum rate of change of the CA transport in each pixel or voxel using a finite difference:

$$CA_{si} = \frac{c(i, t + \Delta t) - c(i, t)}{\Delta t}.$$

Here,  $\Delta t$  represents the sampling rate, and c(i, t) is the ith pixel/voxel concentration value at time t.

It is important to note that the CA is injected at a specific location, leading to dilution where vessels with CA converge with vessels carrying CA-free blood. We performed a pixel- or voxel-wise time-intensity curve analysis to account for this. This involves monitoring intensity changes over time and adjusting for dilution by scaling the intensity with the peak concentration  $I_{\rm max}$  at each pixel or voxel over time.

To facilitate comparisons between the MR Imaging datasets acquired under different parameters and anatomical areas, we normalized the slope  $CA_{si}$  for each pixel/voxel with the overall maximum dispersive slope values to obtain  $CA_{si}^{norm}$ .

Clinically, the rate of signal increase is linked to the steepness of CA wash-in and may reflect whether the CA is traveling through a singular shunting vessel (narrow histogram) or diffusing into multiple venous outflow paths (broader histogram) [27].

The spatial distribution of the above diagnostic parameters is displayed as two-dimensional or three-dimensional colormaps, with values assigned to corresponding pixels or voxels. The statistical distribution of the parameters is displayed by histograms.



# **Statistical Analysis**

For the in vitro validation, we compared the histogram distributions of  ${\rm CA_{ToA}}^{\rm norm}$  and  ${\rm CA_{si}}^{\rm norm}$  for DSA and GRASP through descriptive statistics (mean, standard deviation) and  $\chi^2$  test. We calculated skewness, mean, median, and kurtosis for the histograms of in vivo type II, IV pAVMs, and CV-AVM (Tables 4 and 5).

# Results

#### In Vitro Validation

Figure 2 shows phantom DSA images (t=5 s from the start of acquisition) and selected slices from GRASP imaging (t=96.57 s from the start of acquisition). DSA images provide a sharper contrast of blood vessels and a higher spatial resolution. In MR Imaging, one of the two draining veins is not resolved in two points since it is smaller than the spatial resolution. Video 1 shows the earlier CA arrival using DSA compared to GRASP resulting from the smaller distance between the phantom and the injection point for DSA compared to GRASP.

Colormaps and associated histograms of  $CA_{ToA}^{norm}$  and  $CA_{si}^{norm}$  for the phantom are reported in Fig. 3. The mean value of  $CA_{ToA}^{norm}$  histogram distribution derived from MR imaging is slightly shifted to the left (average = 0.25, std = 0.18) compared to that derived from DSA (average = 0.28, std = 0.24). Despite normalization, the histograms cannot be identical since the 3D case accounts for the extension of the vessels in the third dimension, which gives a significant difference compared to the 2D case. We observe a decrease in the  $CA_{ToA}^{norm}$  histogram distribution at 0.1–0.2 in both imaging modalities, which may represent the low filling of the aneurysmal vein, as observed in Frey et al. [27], but we do not see a second peak in the same histogram distribution representing the veins, due to their small volume.

Table 4 Metrics for CA<sub>ToA</sub>

| ID    | Skewness | Mean  | Median | Kurtosis |
|-------|----------|-------|--------|----------|
| ID001 | 2.24     | 4.40  | 4.59   | 16.90    |
| ID002 | 3.12     | 6.80  | 3.75   | 12.70    |
| ID003 | 6.252    | 11.12 | 10.25  | 51.29    |
| ID006 | 3.62     | 5.76  | 4.51   | 32.12    |
| ID008 | 2.04     | 14.54 | 10.20  | 7.56     |
| ID009 | 2.86     | 18.56 | 15.64  | 13.12    |
| ID012 | 0.92     | 44.90 | 33.81  | 2.50     |
| ID020 | 0.95     | 19.80 | 17.43  | 4.18     |

**Table 5** Metrics for CA<sub>si</sub><sup>norm</sup>

| ID    | Skewness | Mean | Median | Kurtosis |
|-------|----------|------|--------|----------|
| ID001 | -0.12    | 0.46 | 0.45   | 4.00     |
| ID002 | 0.76     | 0.42 | 0.39   | 3.00     |
| ID003 | 0.30     | 0.57 | 0.53   | 2.19     |
| ID006 | 0.69     | 0.36 | 0.31   | 2.71     |
| ID008 | 0.17     | 0.48 | 0.46   | 2.17     |
| ID009 | -0.18    | 0.43 | 0.45   | 2.70     |
| ID012 | 0.27     | 0.49 | 0.50   | 2.70     |
| ID020 | -0.16    | 0.50 | 0.51   | 2.44     |

The histogram of  $CA_{si}^{norm}$  for GRASP reflects the more dispersed bolus for MR Imaging (average = 0.38, std = 0.21) compared to DSA (average = 0.28, std = 0.17). This likely reflects the greater distance between the phantom and the injection point of CA in MR Imaging compared to DSA. However, the  $\chi^2$  test confirms that there is no statistically significant difference between MR-based data and DSA-based data ( $\chi^2$  = 0.20, p = 0.65 for  $CA_{TOA}^{norm}$  and  $\chi^2$  = 0.21, p = 0.65 for  $CA_{si}^{norm}$ ). It can thus be concluded that the histogram distributions show comparable trends.

#### **In Vivo Results**

A representative 3D colormap of CA<sub>ToA</sub> for ID005 is shown in Video 2. The 3D view allows a proper localization of the lesion: the *nidus* appears on the dorsal part of the hand as seen from DSA images, while it appears on the palmar part on the hand when looking at the MR-derived colormap. A figure in the Supplementary Material (Supplementary Material 1) summarizes all histograms of CA<sub>ToA</sub> and CA<sub>si</sub> norm and grouped by type of AVM. In the following sections, each AVM type is separately discussed.

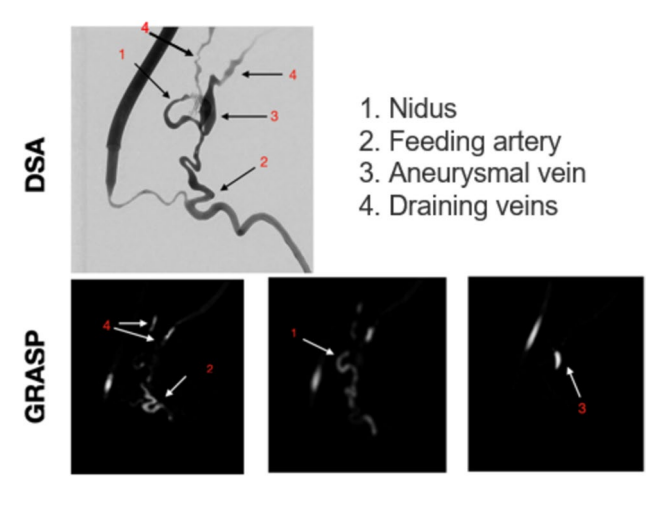


Fig. 2 Selected DSA image and selected slices for GRASP at one time frame, highlighting the main features of the pAVM [30, 36]



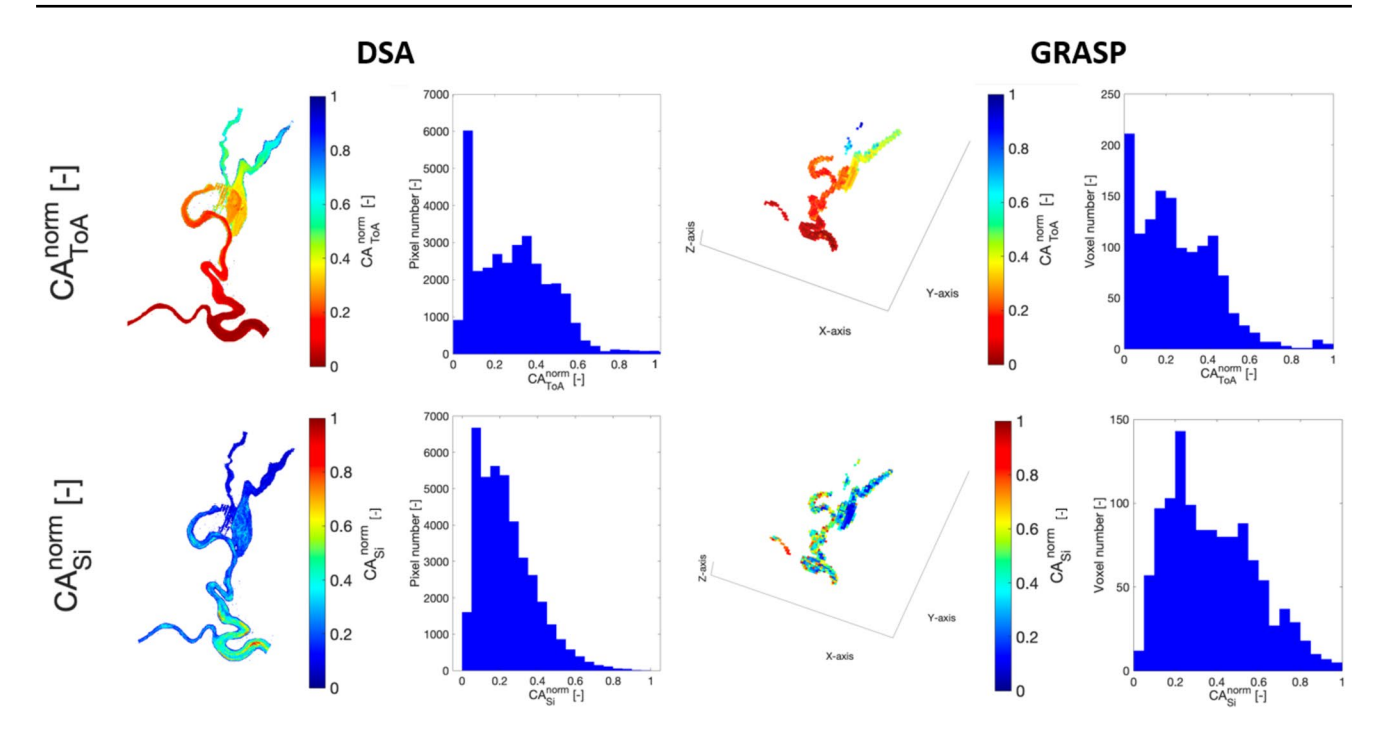


Fig. 3 In vitro results. Spatial distribution and histogram representation of  $CA_{ToA}^{norm}$  (first row) and  $CA_{si}^{norm}$  (second row) obtained from DSA (left column) and GRASP (right column)

# Type II AVM

Figure 4 displays the spatial distributions and associated histograms of  $CA_{ToA}$  and  $CA_{si}^{norm}$  for a type II pAVM (ID001), which anatomically connects multiple arteries or arterioles to a *nidus* with multiple draining veins. The vessels colored red indicate areas with low  $CA_{ToA}$  (representing feeding arteries and high-flow arterio-venous shunts), and vessels colored blue represent areas with high  $CA_{ToA}$  (representing draining veins). The *nidus* is composed of more vessels than feeding arteries and draining veins, which results in a single peak in the  $CA_{ToA}$  histogram corresponding to all intermediate  $CA_{ToA}$  values in the *nidus*.

The  $CA_{ToA}$  histogram exhibits a right-skewed trend, with a single peak at 7 s, a steep decrease, and a short tail, indicating a fast shunting of the lesion with slow wash out. In the central area of the hand, vessels are not distinguishable, and toward the fingers, large cloudy areas are characterized by various  $CA_{ToA}$  values, representing fingers 2 and 3 involved in the lesion. The areas of the colormap that display high  $CA_{ToA}$  values are also characterized by higher  $CA_{si}^{norm}$  values (range between 0.7 and 0.9), which is expected as arteries have higher blood velocities.

The  $CA_{ToA}$  values (Table 4) for ID001 and ID002 both exhibit low skewness values, indicating a moderate right-skewed distribution of  $CA_{ToA}$ . In contrast, ID003 shows a higher skewness, reflecting a pronounced right tail, which indicates the presence of more extreme values in the data.

The lower temporal resolution of ID003 might be the reason for a higher  $CA_{ToA}$  mean and median, which results in metrics more similar to CV-AVM patients. ID003 also has higher median and mean for  $CA_{si}^{norm}$  distribution (Table 5) compared to ID001 and ID002, likely due to the low temporal resolution of the former.

#### Type IIIB AVM

Figure 5 illustrates a type IIIB pAVM (ID004), which is characterized by multiple arteries joining an aneurysmally dilated vein followed by multiple draining veins. The histogram distribution details the circulation in the depicted hand, showing the arterial peak occurring at around 5 s and the broader venous peak at 25 s. The double-peak pattern indicates different hemodynamic characteristics compared to type II, as noted in a previous study by Frey et al., summarized in [5]. This pattern arises from the slower blood flow transition from artery to vein in type IIIB pAVMs, which is attributed to blood retention within the aneurysmal vein and its low filling. The broader venous peak compared to the arterial one is attributed to the large number of interconnected veins before CA reaches the large systemic veins and reflects the highly dispersive venous phase, which is typical of, e.g., type IIIb morphologies that may include multiple, dilated, draining veins.

In contrast, Fig. 6 shows a CA<sub>ToA</sub> histogram (ID005 with a type IIIB pAVM) with a single peak at 15 s. The



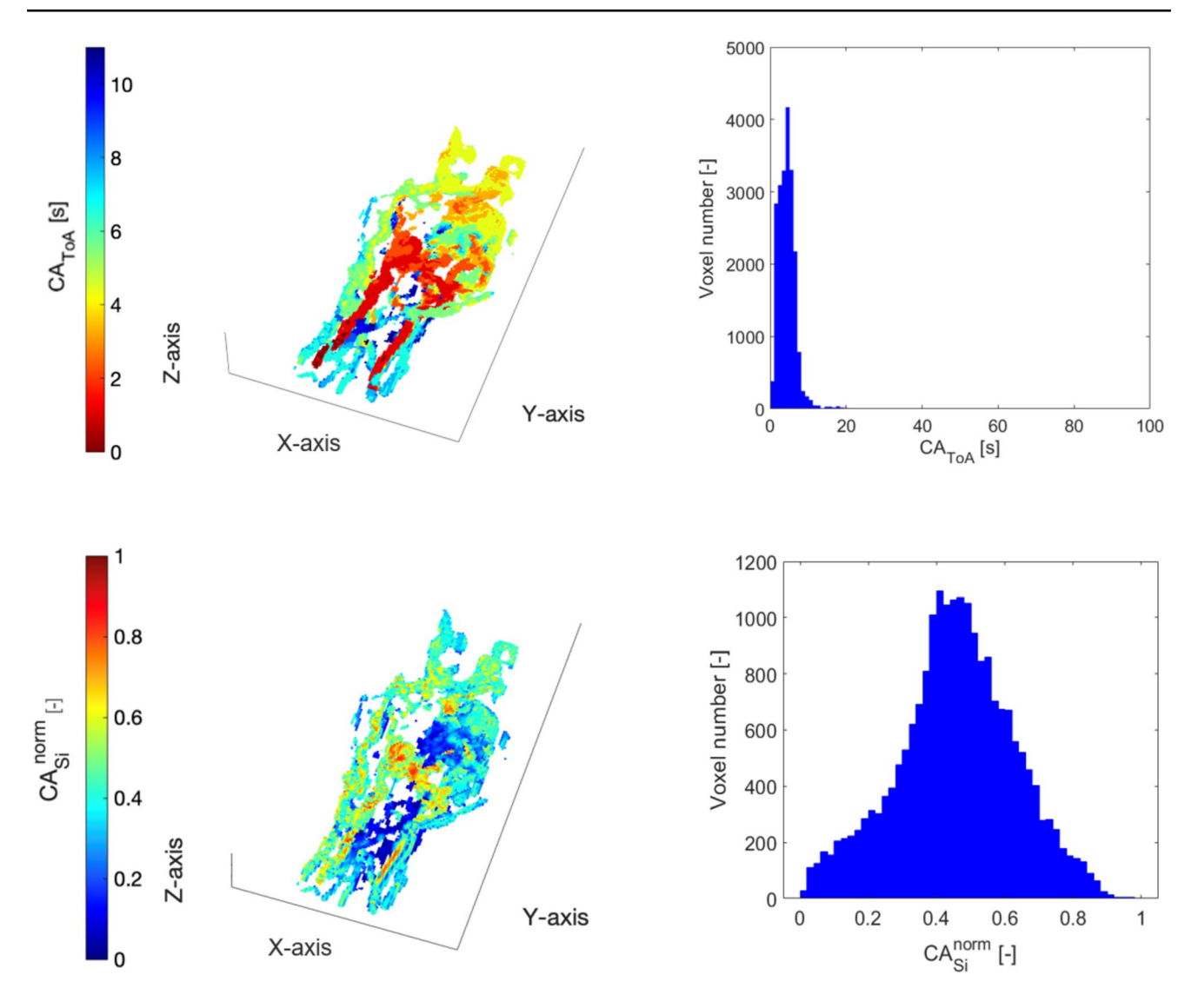


Fig. 4 Type II pAVM, ID001. Spatial distribution (left) and histogram representation (right) of  $CA_{ToA}$  (first row) and  $CA_{si}^{norm}$  (second row) obtained from MR images

absence of the double-peak pattern is likely due to a low temporal resolution, which clusters the bins in a few different values.

Video 2 illustrates a 3D colormap of  $CA_{ToA}$  derived from a CE-trMRA dataset for ID005 (selected patient case) and its comparison with DSA. It highlights the importance of having a 3D mapping of the lesion: the malformation seems to be on the dorsal part of the image on DSA, while it is clear from the 3D colormap derived from CE-trMRA that it is on the palmar part of the hand.

The  $CA_{si}^{\ norm}$  histogram of ID004 exhibits a wide bell shape. On the contrary, a peak at  $CA_{si}^{\ norm}$  = 1 of the histogram is observed in ID005 due to the low temporal resolution, which makes the main feeding artery fill in one time step.

#### Type IV AVM



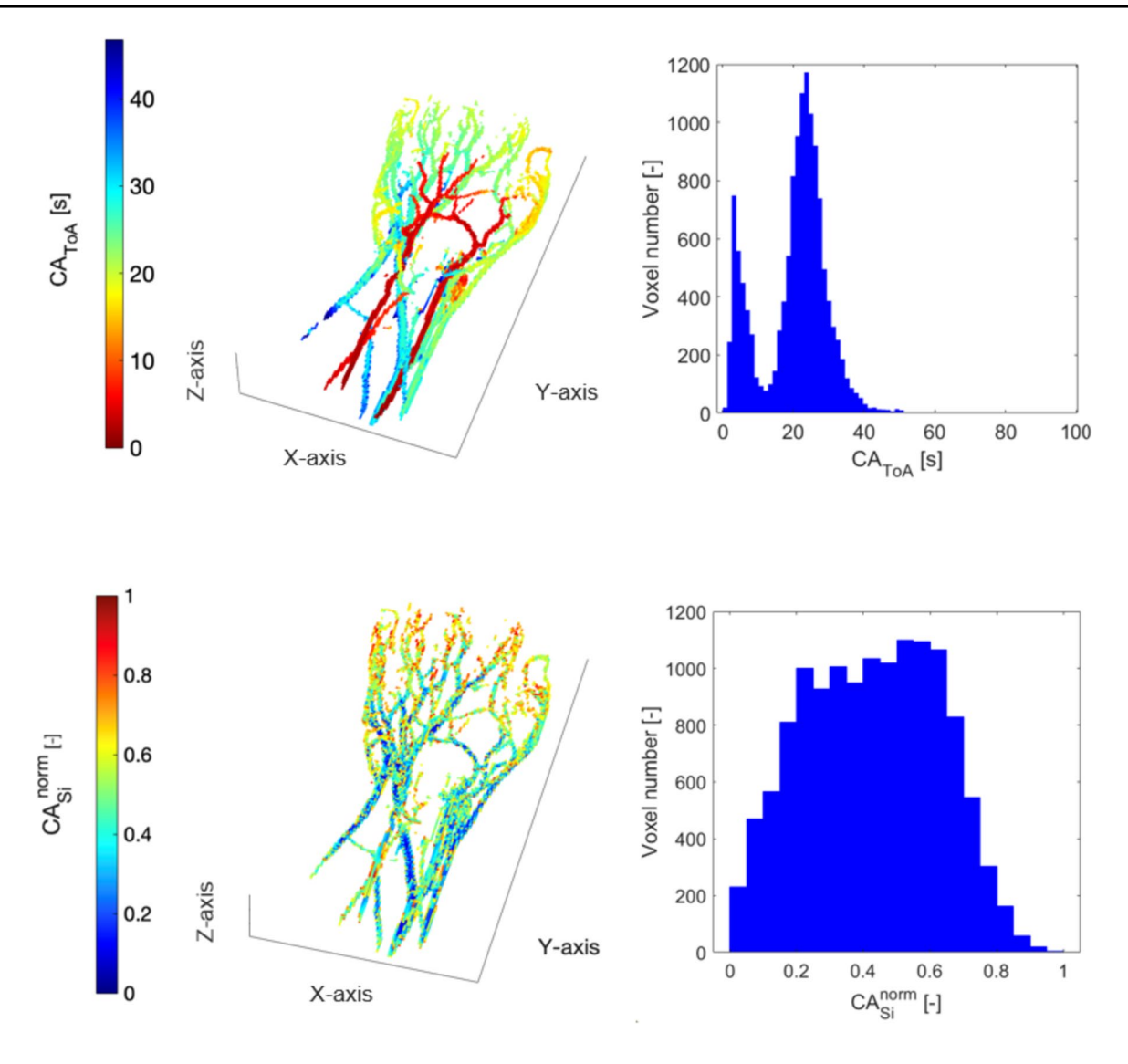


**Fig. 5** Type IIIB pAVM, ID004. Spatial distribution (left) and histogram representation (right) of  $CA_{ToA}$  (first row) and  $CA_{si}^{norm}$  (second row) obtained from MR images. The first peak in the histogram dis-

tribution represents the arteries, the second the veins. The local minimum in the histogram distribution represents the low filling of the aneurysm

The metrics of ID020 for  $CA_{ToA}$  (Table 4) reveal that type IV pAVMs demonstrate a distinct pattern in  $CA_{ToA}$  compared to those in type II. The higher mean and median values suggest slower dynamics, and the moderate skewness value suggests some moderate  $CA_{ToA}$ . The kurtosis values indicate that while ID020 has a relatively moderate distribution, ID001 and ID002 exhibit significant variability with a tendency for extreme values, contrasting with ID003's flatter distribution.

Regarding the metrics of  ${\rm CA_{si}}^{\rm norm}$  (Table 5), the most distinguishing feature of ID020 lies in its skewness and the fact that it exhibits a slight left-skew compared to the positive skewness seen in ID002 and ID003. The kurtosis indicates that while ID020 has a peaked distribution, it does not exhibit extreme values, as in ID001 and ID002.

# Type CV-AVM

Figure 8 shows a CV-AVM, another type of arterio-venous shunting of even smaller diameter of vessels—between capillaries and venules. The colormap of  $CA_{ToA}$  exhibits a wide range of values spanning from red to blue. The histogram shows a higher maximum  $CA_{ToA}$  than all the other pAVM types, with values reaching more than 100 s. The histogram pattern exhibits an initial peak around 12 s; then it decreases gradually up to 70 s while exhibiting a right-skewness. Subsequently, a second section shows an area of high  $CA_{ToA}$ . The longer acquisition times of CE-trMRA allow us to observe a tail of values, which likely represents delayed venous return.



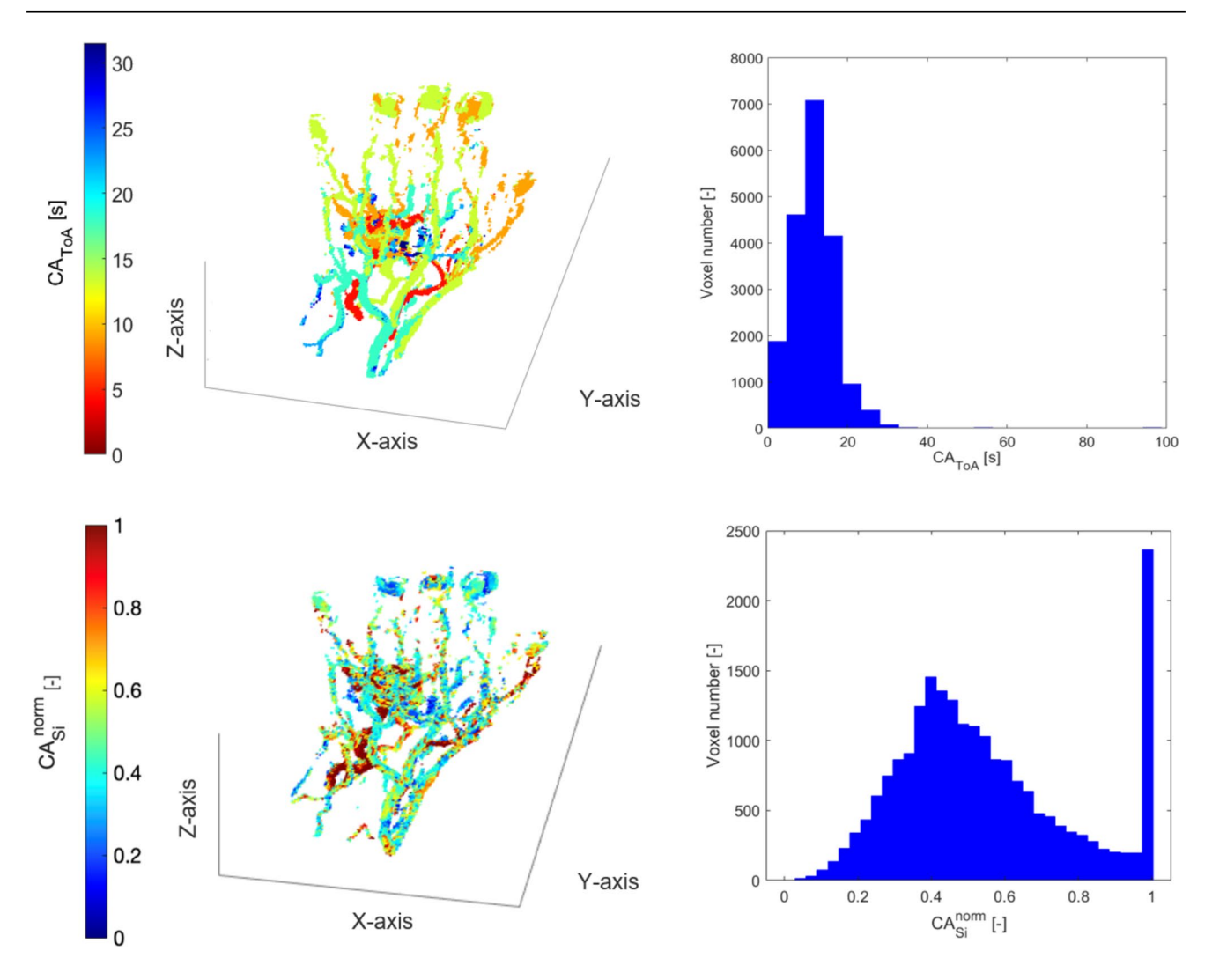


Fig. 6 Type IIIB pAVM, ID005. Spatial distribution (left) and histogram representation (right) of  $CA_{ToA}$  (first row) and  $CA_{si}^{norm}$  (second row) obtained from MR images

The CA<sub>ToA</sub> distribution for patients diagnosed with CV-AVM varies, with the first peak generally appearing less right-skewed compared to type IV malformations. CV-AVM patients are distinguished by their higher mean and median values of CA<sub>ToA</sub> (Table 4) compared to other pAVM types, reflecting a broader and skewed distribution toward higher values. The skewed nature toward higher values reflects the broader spread and highlights the presence of higher central values in CV-AVMs. The CA<sub>si</sub> norm metrics for CV-AVMs (Table 5) show mild skewness with a slight negative or positive trend. Kurtosis values varying between 2.40 and 2.70 indicate normal distributions with light tails. The mean and median values are quite consistent, which suggests symmetric distributions.

Generally, types II and III pAVMs show more variability in the distributions of  $CA_{si}^{\quad norm}$ , while CV-AVMs and type IV pAVMs exhibit more uniform and symmetric distributions.

# **Discussion**

In this work, we present a set of diagnostic parameters indicative of the type of pAVMs, which can be measured from MR Imaging. The study is divided into two parts. The in vitro part serves as a validation of the hemodynamic markers previously computed [27] and characterizes pAVMs in DSA and MR environments. The in vivo part investigates the feasibility of characterizing hemodynamic parameters of in vivo pAVMs through CE-trMRA datasets and explores the clinical advantages of using MR Imaging compared to DSA. This characterization is achieved by analyzing the CA transport parameters, i.e., by computing the time required for CA to appear at a certain location (CA<sub>TOA</sub>) and the local rate of CA-signal increase (CA<sub>si</sub><sup>norm</sup>).



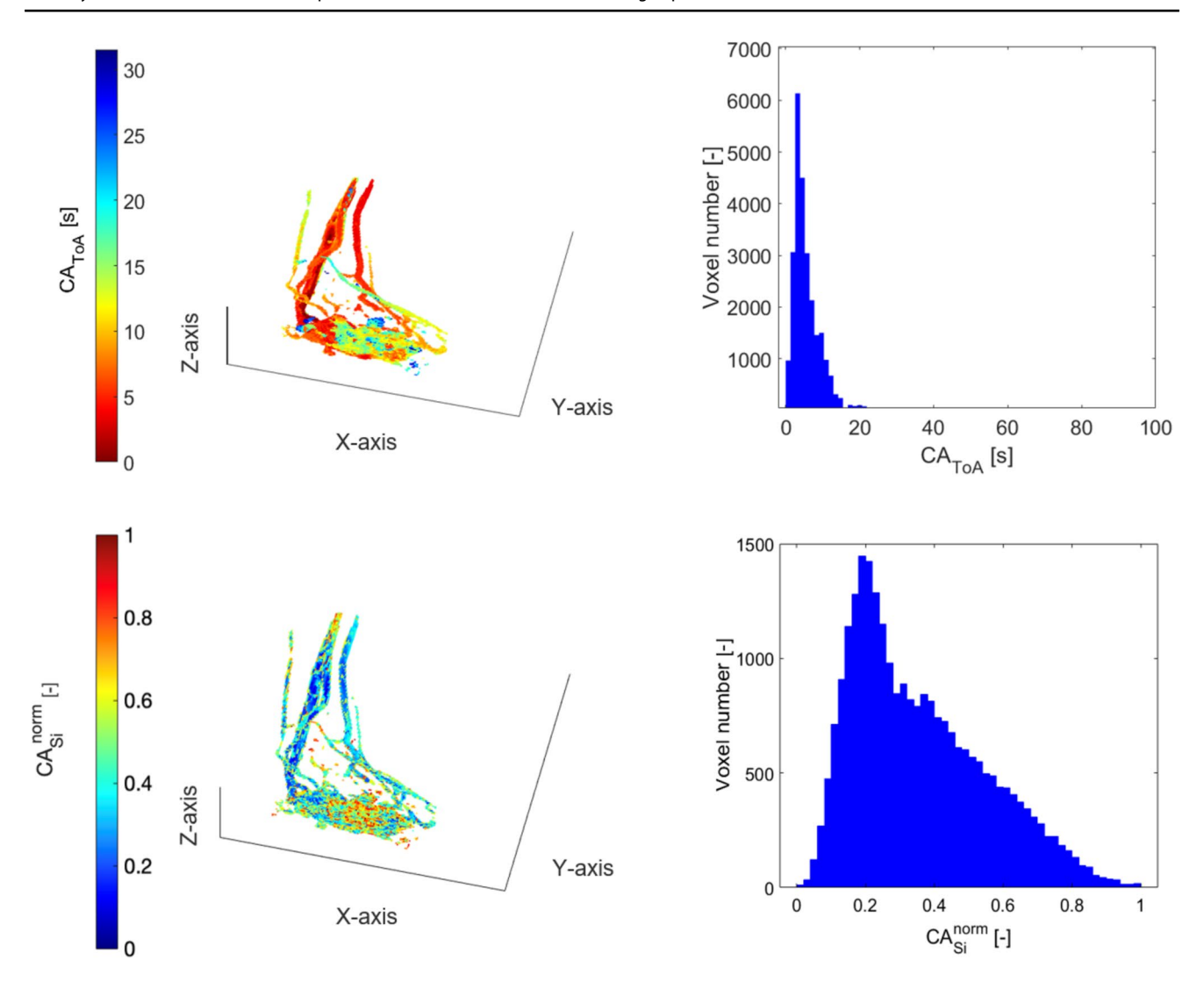


Fig. 7 Type IV pAVM, ID006. Spatial distribution (left) and histogram representation (right) of  $CA_{ToA}$  (first row) and  $CA_{si}^{norm}$  (second row) obtained from MR images

# **In Vitro Validation**

We validated the proposed hemodynamic markers using controlled in vitro experiments comparing DSA and MR Imaging in a 3D-printed phantom. The  $CA_{ToA}^{norm}$  histogram from MR Imaging (mean = 0.25, std = 0.18) closely resembled that from DSA (mean = 0.28, std = 0.24). Similarly,  $CA_{si}^{norm}$  from MR Imaging (mean = 0.38, std = 0.21) showed dispersion patterns comparable to DSA (mean = 0.28, std = 0.17) and reflects the effect of different injection protocols. Although  $CA_{si}^{norm}$  is well suited to characterize the dispersivity of the lesions, this hemodynamic marker is strongly dependent on the injection protocol. Hence, the broader histogram of  $CA_{si}^{norm}$  derived from MR Imaging compared to DSA is expected as a result of the larger distance between injection point and phantom that mimics the intra-arterial injection in

DSA and the intra-venous injection in MR Imaging environments. Despite differences in acquisition setups, the  $\chi^2$  test confirmed no statistically significant differences in histogram distributions (CA<sub>ToA</sub> norm:  $\chi^2 = 0.20$ , p = 0.65; CA<sub>si</sub> norm:  $\chi^2 = 0.21$ , p = 0.65), validating the transferability of the hemodynamic markers to MR-based classification.

The validation of the proposed pAVM hemodynamic markers [27] to characterize pAVMs through controlled experiments, MR Imaging and DSA, provides, to the best of our knowledge, the first experimental set-up of a detailed model of a pAVM with fully known geometry of the lesion and surrounding vasculature, using clinical imaging modalities. This validation establishes a foundation for its application into clinical practice, where it can be used to analyze blood flow dynamics and to develop new diagnostic and therapeutic markers, eventually to optimize treatment strategies and improve patient outcomes.



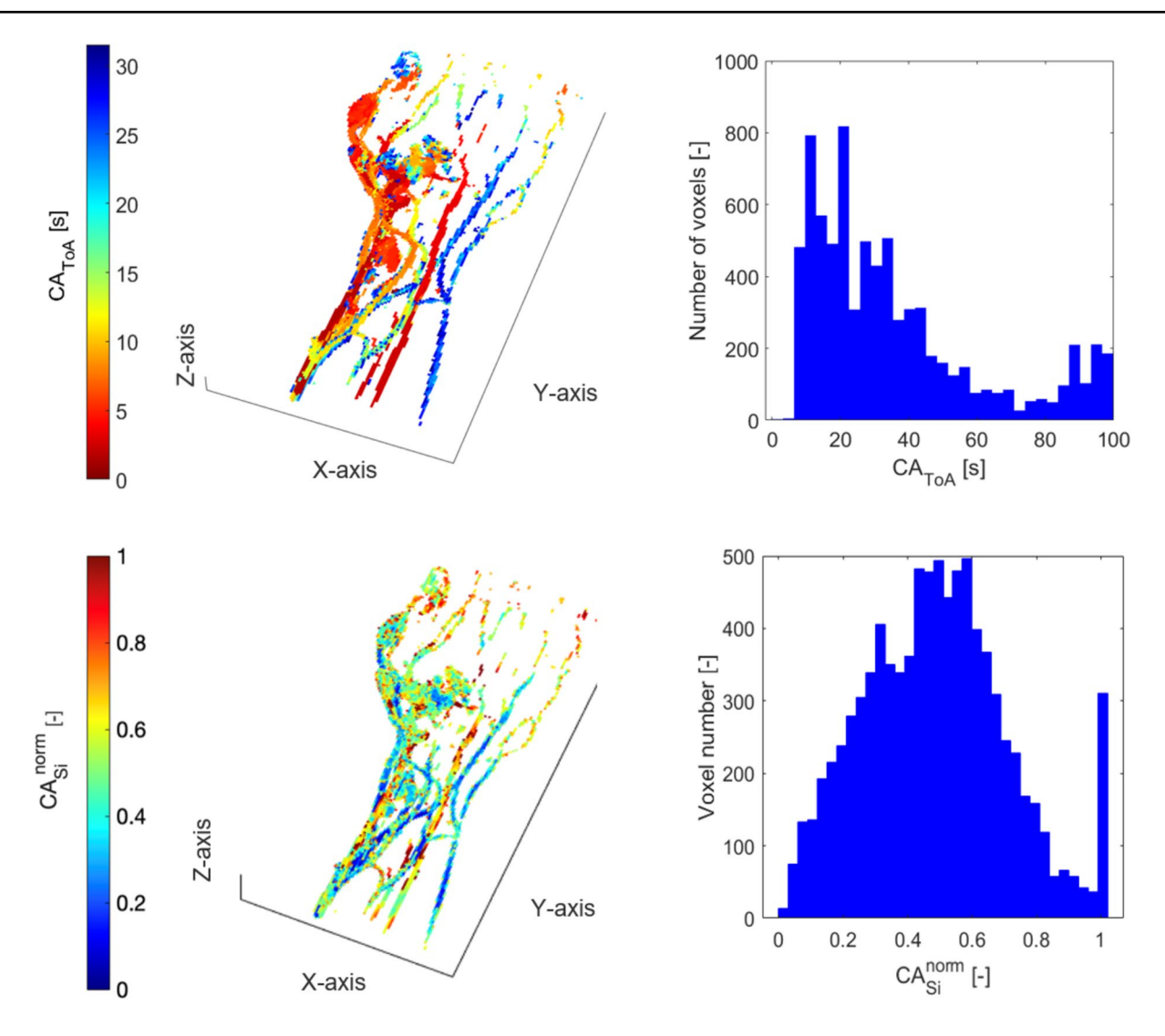


Fig. 8 CV-AVM, ID012. Spatial distribution (left) and histogram representation (right) of  $CA_{ToA}$  (first row) and  $CA_{si}^{norm}$  (second row) obtained from MR images

# **Application of the Metrics to In Vivo Data**

# Time of Arrival (CA<sub>ToA</sub>)

The image processing on the in vivo MR image datasets of extremities shows that  $CA_{ToA}$  is a powerful hemodynamic parameter for the classification of pAVMs. The histogram shapes of  $CA_{ToA}$  are able to capture local blood flow velocities, shunting behaviors, and hemodynamic characteristics of the pAVM types.

We found that the spatial distributions (colormaps) and histogram representations for  $CA_{ToA}$  with sufficiently high MR acquisition parameters align with trends previously observed computationally and DSA recordings [5]. Interestingly, MR Imaging is able to distinguish CV-AVMs by the presence of peaks in the  $CA_{ToA}$  histogram around 100 s, a feature which would not be extracted from DSA images

where venous return visualization is limited, and scans often end prematurely to limit radiation exposure. This suggests that late  $CA_{ToA}$  could be a clinically relevant indicator for identifying CV-AVMs among other pAVM types.

For clinicians, knowledge of the distribution of  $CA_{ToA}$  in the lesion and the surrounding vessels provides an indication of the types of blood vessels affected by the malformation: late arrival times suggest the presence of microvascular pAVMs with higher resistance than lesions in large vessels that exhibit early arrival times. In addition, distinguishing between normalized and non-normalized  $CA_{ToA}$  is crucial for clinicians. While normalized  $CA_{ToA}$  spatial distributions and histograms allow for comparative analysis across different images, non-normalized  $CA_{ToA}$  colormaps and histograms provide clinicians with precise temporal information to identify blood flow abnormalities. Such information can be an indicator of the lesion size, the role of the lesion within



other vascular structures, and hence used to monitor treatment progress.

# Dispersive Slope (CA<sub>si</sub>)

The right-skewed histogram and higher dispersive upslope values of microcirculatory type IV pAVM compared to types II and III may primarily arise from the extensive network of shunting vessels and pathological connections with low dispersion areas characteristic of type IV, resulting in lower dispersive slope values and shifting the histogram toward lower CA<sub>si</sub> norm values.

Interestingly, CV-AVMs do not exhibit a consistent trend in the  $CA_{si}^{\quad norm}$  histograms computed from CE-trMRA. While greater dispersion and low  $CA_{si}^{\quad norm}$  values might be expected due to microcirculation, this is not observed, likely due to the absence of a *nidus* and the limited spatial resolution of CE-trMRA.

#### **General Considerations**

We have shown that our MR-based datasets with a temporal resolution around 1 s can provide a detailed characterization of CA distribution patterns and dynamics and provide sufficient temporal detail to distinguish between different pAVM types, supporting lesion characterization.

MR-based datasets with lower temporal resolution cannot capture important hemodynamic information and do not show an accurate histogram classification. For example, for patients ID005 and ID012, we see that in the  ${\rm CA_{si}}^{\rm norm}$ , there is a peak at unity, which represents the filling of the arteries in one time step. This observation does not hold for the  ${\rm CA_{ToA}}$  of ID012 (CV-AVM) because we focus on the presence of late  ${\rm CA_{ToA}}$ , which is not affected by the temporal resolution.

Another acquisition parameter which has to be considered is the spatial resolution, crucial for precise vessel visualization. CE-trMRA typically has lower spatial resolution compared to DSA, leading to the inability to visualize small blood vessels and partial volume effects [44]. This can blur fine anatomical details, e.g., in CV-AVM and not allow the differentiation of adjacent small vessels as voxels blend blood vessels with the surrounding tissue. Slice thickness impacts the quality of 3D rendering too: smaller slice thickness reduces small gaps and stair-steps artifacts between slices and contributes to smoother 3D visualizations, producing a more continuous and detailed representation of vascular structures.

DSA has limitations despite its ability to visualize pAVM development over time. Firstly, it is invasive in its injection method, requiring a catheter for intravascular access. In contrast, even with a peripheral injection, our MR Imaging approach still yields high-quality histograms.

In addition, DSA provides a two-dimensional colormap due to single-projection imaging, which can miscalculate diagnostic parameters where veins and arteries overlap. This limitation hinders understanding of the three-dimensional angioarchitecture (location, size, and shape of the malformation to be treated), which is essential for accurate clinical diagnosis and treatment planning [49, 50]. The 3D colormaps provide diagnostic aids, allowing clinicians to have a quick 3D visualization of the pAVM morphology and facilitate arterio-venous separation, as shown by Schubert et al. [51] for cAVMs and efficient localization of hemodynamic hotspots (e.g., *nidus*) in the 3D space [52]. For instance, in ID001, the 3D colormap provides the physicians a quick understanding that fingers 1, 4, and 5 have poor perfusion due to a steal phenomenon.

Finally, the longer scan time of CE-trMRA compared to DSA may improve the detection of microvascular AVMs that would otherwise remain unnoticed on shorter DSA acquisitions. This could support more accurate lesion classification and improved treatment planning.

Our findings have a substantial impact on pAVM diagnosis, since they may allow an automated classification of lesions, solely based on the analysis of radiation-free MR images, which may reduce the number of misdiagnoses of pAVMs and may improve personalized treatment. Although we did not perform a diagnostic accuracy or clinical utility study, this study clearly supports the use of MR imaging as primary tool for baseline diagnostics and follow-up. This recommendation aligns with the results reported in [53–55], which suggest that additional diagnostic DSA is not required for treatment planning prior to therapeutic endovascular procedures.

The proposed classification framework for pAVM can be adapted to characterize pAVMs of other anatomical areas. A different trade-off between spatial and temporal resolution might be established for different body regions. Using a radial sequence might be beneficial in terms of better vascular contrast, vessel sharpness, and motion robustness for pAVM in the body's abdominal region [56]. However, this is beyond the scope of the present study.

## Limitations

The present study has highlighted the use of MR Imaging extracted CA-based metrics for the classification of pAVMs. A relatively small number of datasets were employed, limited to a specific body anatomy. Furthermore, the study did not include type I and IIIa pAVMs because MR datasets were not available for these types.

Another limitation of the study is the low in-plane spatial resolution of the MR datasets that did not allow sub-millimeter vessels to be distinguished and relevant hemodynamic features to be identified. Further improvements in



MR Imaging acquisition parameters might be required to fully replace DSA in diagnosing pAVMs.

Further work might be needed to fully assess and quantify the impact on injection on  ${\rm CA_{si}}^{\rm norm}$  as studies show varying results between the injected GBCA volume and injection rate, and the concentration and the signal intensity [57–61]. Thus, our results for  ${\rm CA_{si}}^{\rm norm}$  might be dependent on such injection parameters.

Additionally, the use of a finite difference approximation to compute the  ${\rm CA_{si}}^{\rm norm}$  introduces sensitivity to the temporal resolution of the acquisition. Low temporal resolution may result in underestimation or oversimplification of the true CA dynamics, especially in vessels where contrast changes rapidly. This should be considered when interpreting and comparing  ${\rm CA_{si}}^{\rm norm}$  metrics across datasets with different acquisition settings.

#### **Conclusions**

We have shown that MR Imaging allows the estimation of CA transport parameters such as  ${\rm CA_{ToA}}$  and  ${\rm CA_{si}}^{\rm norm}$  in both in vitro and in vivo datasets, allowing to characterize different types of pAVMs without the need of DSA. The characterization of pAVMs through such hemodynamic markers has the potential to become a diagnostic procedure for the surgical navigation and classification of pAVMs for clinicians. In the future, this approach could enhance diagnostic precision, guide the development of more effective treatment strategies, and help reduce the complication rates and the incidence of misdiagnosed cases.

**Supplementary Information** The online version contains supplementary material available at https://doi.org/10.1007/s10439-025-03766-3.

Acknowledgments This study was funded by the Swiss National Foundation, Sinergia CRSII5\_193694. We also gratefully acknowledge the financial support of the Butterfly AVM Charity, the CDI AWS Doctoral Scholarship, the Biotechnology and Biological Sciences research Council (BBSRC) International Institution Awards to UCL, UK Research and Innovation (UKRI, BB/X005062/1) MEDICARE and Welcome/EPSRC Centre for Interventional and Surgical Sciences (WEISS) (2031145Z/16/Z). The in vitro patient data were obtained at Royal Free Hospital (London, UK) by clinicians Chung Sim Lim and Janice Tsui with support from the National Institute for Health Research, University College London Hospitals Biomedical Research Centre. We thank Theofilos Boulafentis and Anastasios Koulogiannis for the support in the experiments.

Author Contributions Conceptualization: CGC, MB, DO, HvTK, BJ. Methodology: CGC, ABG. Investigation: CGC. Formal analysis: CGC, MB. Validation: CGC, ABG, AT. Supervision: DO, HvTK, BJ. Resources: HvTK. Writing—first draft: CGC. Writing—review and editing: CGC, ABG, SMB, VDZ, SB, DO, HvTK, BJ.

Funding Open access funding provided by University of Bern.



#### **Declarations**

Conflict of interest None declared.

Open Access This article is licensed under a Creative Commons Attribution 4.0 International License, which permits use, sharing, adaptation, distribution and reproduction in any medium or format, as long as you give appropriate credit to the original author(s) and the source, provide a link to the Creative Commons licence, and indicate if changes were made. The images or other third party material in this article are included in the article's Creative Commons licence, unless indicated otherwise in a credit line to the material. If material is not included in the article's Creative Commons licence and your intended use is not permitted by statutory regulation or exceeds the permitted use, you will need to obtain permission directly from the copyright holder. To view a copy of this licence, visit http://creativecommons.org/licenses/by/4.0/.

# References

- Enjolras, O., M. Wassef, and R. Chapot. Color Atlas of Vascular Tumors and Vascular Malformations, 1st ed. Cambridge: Cambridge University Press, 2007.
- Cox, J. A., E. Bartlet, and E. I. Lee. Vascular malformations: a review. Semin. Plast. Surg. 28(2):58–63, 2014. https://doi.org/ 10.1055/s-0034-1376263.
- Tasnádi, G. Epidemiology and etiology of congenital vascular malformations. Semin. Vasc. Surg. 6(4):200–203, 1993.
- International Society for the Study of Vascular Anomalies, https://www.issva.org
- Von Tengg-Kobligk, H., S. Frey, D. Obrist, and I. Baumgartner. Arteriographic assessment: is it still the gold standard for diagnosis of arteriovenous malformations? In: Vascular Malformations, 1st ed. Boca Raton: CRC Press, 2019, pp. 69–72.
- Strübing, F. F., S. Porubsky, A. K. Bigdeli, V. J. Schmidt, L. Krebs, U. Kneser, and M. Sadick. Interdisciplinary management of peripheral arteriovenous malformations: review of the literature and current proceedings. *J. Plast. Surg. Hand Surg.* 56(1):1–10, 2022. https://doi.org/10.1080/2000656X.2021. 1913743.
- Flors, L., C. Leiva-Salinas, I. M. Maged, P. T. Norton, A. H. Matsumoto, J. F. Angle, H. Bonatti, A. W. Park, E. A. Ahmad, U. Bozlar, A. M. Housseini, T. E. Huerta, and K. D. Hagspiel. MR imaging of soft-tissue vascular malformations: diagnosis, classification, and therapy follow-up. *Radiographics*. 31(5):1321–1340, 2011. https://doi.org/10.1148/rg.315105213.
- Yakes, W., and I. Baumgartner. Interventional treatment of arterio-venous malformations. *Gefaesschirurgie*. 19:325–330, 2014. https://doi.org/10.1007/s00772-013-1303-9.
- Yakes, W. F., and A. M. Yakes. Classification of arteriovenous malformation and therapeutic implication. In: *Hemangiomas and Vascular Malformations*. Milan: Springer, 2015, pp. 263–276.
- Frey, S., T. Cantieni, N. Vuillemin, A. Haine, R. Kammer, H. von Tengg-Kobligk, D. Obrist, and I. Baumgartner. Angioarchitecture and hemodynamics of microvascular arterio-venous malformations. *PLoS ONE*. 2018. https://doi.org/10.1371/journal.pone.0203368.
- Vuillemin, N., S. Bernhard, M. Schindewolf, D. Häberli, U. Hügel, D. Obrist, and I. Baumgartner. Capillary-venulous malformation a microfistular variant of arteriovenous malformation.
   J. Vasc. Surg. 2021. https://doi.org/10.1016/j.jvsv.2020.05.012.
- Wong, K. K., D. Wang, J. K. Ko, J. Mazumdar, T.-T. Le, and D. Ghista. Computational medical imaging and hemodynamics framework for functional analysis and assessment of

- cardiovascular structures. *Biomed. Eng. Online*. 16:35, 2017. https://doi.org/10.1186/s12938-017-0326-y.
- Peper, E. S., P. van Ooij, B. Jung, A. Huber, C. Gräni, and J. A. M. Bastiaansen. Advances in machine learning applications for cardiovascular 4D flow MRI. Front. Cardiovasc. Med. 9:1052068, 2022. https://doi.org/10.3389/fcvm.2022.1052068.
- Kadem, M., L. Garber, M. Abdelkhalek, B. K. Al-Khazraji, and Z. Keshavarz-Motamed. Hemodynamic modeling, medical imaging, and machine learning and their applications to cardiovascular interventions. *IEEE Rev. Biomed. Eng.* 16:403–420, 2023. https://doi.org/10.1109/RBME.2022.3142058.
- Stokes, C., D. Ahmed, N. Lind, F. Haupt, D. Becker, J. Hamilton, V. Muthurangu, H. von Tengg-Kobligk, G. Papadakis, S. Balabani, and V. Díaz-Zuccarini. Aneurysmal growth in type-B aortic dissection: assessing the impact of patient-specific inlet conditions on key haemodynamic indices. *J. R. Soc. Interface*. 20:20230281, 2023. https://doi.org/10.1098/rsif.2023.0281.
- Zhu, Y., X. Y. Xu, U. Rosendahl, J. Pepper, and S. Mirsadraee. Advanced risk prediction for aortic dissection patients using imaging-based computational flow analysis. *Clin. Radiol.* 78:e155–e165, 2023. https://doi.org/10.1016/j.crad.2022.12. 001.
- Franzetti, G., M. Bonfanti, S. Homer-Vanniasinkam, V. Díaz-Zuccarini, and S. Balabani. Experimental evaluation of the patient-specific haemodynamics of an aortic dissection model using particle image velocimetry. *J. Biomech*. 134:110963, 2022. https://doi.org/10.1016/j.jbiomech.2022.110963.
- Trojan, M., F. Rengier, D. Kotelis, M. Müller-Eschner, S. Partovi, C. Fink, C. Karmonik, D. Böckler, H. U. Kauczor, and H. von Tengg-Kobligk. Time-resolved three-dimensional contrastenhanced magnetic resonance angiography in patients with chronic expanding and stable aortic dissections. *Contrast Media Mol. Imaging*. 2017:5428914, 2017. https://doi.org/10.1155/2017/5428914.
- Nørgaard, B. L., J. Leipsic, B.-K. Koo, C. K. Zarins, J. M. Jensen, N. P. Sand, and C. A. Taylor. Coronary computed tomography angiography derived fractional flow reserve and plaque stress. *Curr. Cardiovasc. Imaging Rep.* 9:2, 2016. https://doi.org/10. 1007/s12410-015-9366-5.
- Ninno, F., C. Chiastra, M. Colombo, A. Dardik, D. Strosberg, E. Aboian, J. Tsui, M. Bartlett, S. Balabani, and V. Díaz-Zuccarini. Modelling lower-limb peripheral arterial disease using clinically available datasets: impact of inflow boundary conditions on hemodynamic indices for restenosis prediction. *Comput. Methods Programs Biomed*.251:108214, 2024. https://doi.org/10.1016/j.cmpb. 2024.108214.
- Rayz, V. L., and A. A. Cohen-Gadol. Hemodynamics of cerebral aneurysms: connecting medical imaging and biomechanical analysis. *Annu. Rev. Biomed. Eng.* 22:231–256, 2020. https://doi.org/ 10.1146/annurev-bioeng-092419-061429.
- Gao, E., W. L. Young, G. J. Hademenos, T. F. Massoud, R. R. Sciacca, Q. Ma, S. Joshi, H. Mast, J. P. Mohr, S. Vulliemoz, and J. Pile-Spellman. Theoretical modelling of arteriovenous malformation rupture risk: a feasibility and validation study. *Med. Eng. Phys.* 20(7):489–501, 1998. https://doi.org/10.1016/s1350-4533(98)00059-9.
- Hademenos, G. J., and T. F. Massoud. Risk of intracranial arteriovenous malformation rupture due to venous drainage impairment. A theoretical analysis. *Stroke*. 27(6):1072–1083, 1996. https://doi. org/10.1161/01.str.27.6.1072.
- Golovin, S. V., A. K. Khe, and K. A. Gadylshina. Hydraulic model of cerebral arteriovenous malformation. *J Fluid Mech.* 797:110– 129, 2016. https://doi.org/10.1017/jfm.2016.245.
- Yu, Y., and D. Y. T. Chen. Chapter 29: machine learning for cerebrovascular disorders. In: Machine Learning for Brain Disorders, edited by O. Colliot. New York: Humana, 2023.

- Jabal, M. S., M. A. Mohammed, C. L. Nesvick, et al. DSA quantitative analysis and predictive modeling of obliteration in cerebral AVM following stereotactic radiosurgery. *Am. J. Neuroradiol.* 2024. https://doi.org/10.3174/ajnr.A8351. (Published online September 2024)
- Frey, S., A. Haine, R. Kammer, H. von Tengg-Kobligk, D. Obrist, and I. Baumgartner. Hemodynamic characterization of peripheral arterio-venous malformations. *Ann. Biomed. Eng.* 45(6):1449– 1461, 2017. https://doi.org/10.1007/s10439-017-1821-9.
- Gülan, U., B. Lüthi, M. Holzner, A. Liberzon, A. Tsinober, and W. Kinzelbach. Experimental study of aortic flow in the ascending aorta via particle tracking velocimetry. *Exp. Fluids*. 53:1469–1485, 2012. https://doi.org/10.1007/s00348-012-1371-8.
- Brindise, M. C., S. Rothenberger, B. Dickerhoff, S. Schnell, M. Markl, D. Saloner, V. L. Rayz, and P. P. Vlachos. Multi-modality cerebral aneurysm haemodynamic analysis: in vivo 4D flow MRI, in vitro volumetric particle velocimetry and in silico computational fluid dynamics. *J. R. Soc. Interface*. 16:20190465, 2019. https://doi.org/10.1098/rsif.2019.0465.
- Franzetti, G., M. Bonfanti, C. Tanade, L. Sim, J. Tsui, G. Hamilton, V. Díaz-Zuccarini, and S. S. Balabani. Computational framework for pre-interventional planning of peripheral arteriovenous malformations. *Cardiovasc. Eng. Technol.* 13(2):234–246, 2022. https://doi.org/10.1007/s13239-021-00572-.
- Ku, J. P., C. J. Elkins, and C. A. Taylor. Comparison of CFD and MRI flow and velocities in an in vitro large artery bypass graft model. *Ann. Biomed. Eng.* 33(3):257–269, 2005. https://doi.org/10.1007/s10439-005-1729-7.
- Boutsianis, E., H. Dave, T. Frauenfelder, D. Poulikakos, S. Wildermuth, M. Turina, Y. Ventikos, and G. Zünd. Computational simulation of intracoronary flow based on real coronary geometry. *Eur. J. Cardiothorac. Surg.* 26(2):248–256, 2004. https://doi.org/10.1016/j.ejcts.2004.02.041.
- 33. Bock, J., J. Töger, S. Bidhult, K. Markenroth Bloch, P. Arvidsson, M. Kanski, H. Arheden, F. Testud, A. Greiser, E. Heiberg, and M. Carlsson. Validation and reproducibility of cardiovascular 4D-flow MRI from two vendors using 2 × 2 parallel imaging acceleration in pulsatile flow phantom and in vivo with and without respiratory gating. *Acta Radiol.* 60(3):327–337, 2019. https://doi.org/10.1177/0284185118784981.
- 34. Töger, J., P. M. Arvidsson, J. Bock, M. Kanski, G. Pedrizzetti, M. Carlsson, H. Arheden, and E. Heiberg. Hemodynamic forces in the left and right ventricles of the human heart using 4D flow magnetic resonance imaging: phantom validation, reproducibility, sensitivity to respiratory gating and free analysis software. *PLoS ONE*.13(4):e0195597, 2018. https://doi.org/10.1371/journ al.pone.0195597.
- Kaneko, N., H. Ullman, F. Ali, P. Berg, Y. C. Ooi, S. Tateshima, G. P. Colby, Y. Komuro, P. Hu, K. Khatibi, et al. In vitro modeling of human brain arteriovenous malformation for endovascular simulation and flow analysis. *World Neurosurg*. 141:e873–e879, 2020. https://doi.org/10.1016/j.wneu.2020.06.084.
- Blanch-Granada, A., T. Boulafentis, L. C. Sim, J. Tsui, V. Diaz-Zuccarini, and S. Balabani. In vitro characterisation of the patient-specific haemodynamics of an extracranial peripheral arteriovenous malformation using PIV. *J Biomech.* 183:112604, 2025. https://doi.org/10.1016/j.jbiomech.2025.112604.
- Huf, V. I., C. Fellner, W. A. Wohlgemuth, C. Stroszczynski, M. Schmidt, C. Forman, J. Wetzl, and W. Uller. Fast TWIST with iterative reconstruction improves diagnostic accuracy of AVM of the hand. Sci. Rep. 10(1):16355, 2020. https://doi.org/10.1038/s41598-020-73331-6.
- Katscher, U., and P. Börnert. Parallel magnetic resonance imaging. *Neurotherapeutics*. 4(3):499–510, 2007. https://doi.org/10.1016/j.nurt.2007.04.01.



- Deshmane, A., V. Gulani, M. A. Griswold, and N. Seiberlich. Parallel MR imaging. J. Magn. Reson. Imaging. 36(1):55–72, 2012. https://doi.org/10.1002/jmri.23639.
- Hamilton, J., D. Franson, and N. Seiberlich. Recent advances in parallel imaging for MRI. *Prog. Nucl. Magn. Reson. Spectrosc.* 101:71–95, 2017. https://doi.org/10.1016/j.pnmrs.2017.04.002.
- Larkman, D. J., and R. G. Nunes. Parallel magnetic resonance imaging. *Phys. Med. Biol.* 2007. https://doi.org/10.1088/0031-9155/52/7/R01.
- Griswold, M. A., S. Kannengiesser, R. M. Heidemann, J. Wang, and P. M. Jakob. Field-of-view limitations in parallel imaging. *Magn. Reson. Med.* 52(5):1118–1126, 2004. https://doi.org/10.1002/mrm.20249.
- Jaspan, O. N., R. Fleysher, and M. L. Lipton. Compressed sensing MRI: a review of the clinical literature. *Br. J. Radiol.* 88(1056):20150487, 2015. https://doi.org/10.1259/bjr.20150 487
- Lustig, M., D. Donoho, and J. M. Pauly. Sparse MRI: the application of compressed sensing for rapid MR imaging. *Magn. Reson. Med.* 58(6):1182–1195, 2007. https://doi.org/10.1002/mrm.21391.
- Feng, L., T. Benkert, K. T. Block, D. K. Sodickson, R. Otazo, and H. Chandarana. Compressed sensing for body MRI. *J. Magn. Reson. Imaging*. 45(4):966–987, 2017. https://doi.org/10.1002/jmri.25547.
- Block, K. T., M. Uecker, and J. Frahm. Undersampled radial MRI with multiple coils: iterative image reconstruction using a total variation constraint. *Magn. Reson. Med.* 57(6):1086–1098, 2007. https://doi.org/10.1002/mrm.21236.
- 47. Nielsen, J. Probing the fractal structure of grey matter dendrite networks using high frequency oscillating gradient diffusion weighted MRI. Master's Thesis. Copenhagen University Hospital Hvidovre and Danish Research Centre for Magnetic Resonance, 2015
- Holdsworth, D. W., C. J. Norley, R. Frayne, D. A. Steinman, and B. K. Rutt. Characterization of common carotid artery blood-flow waveforms in normal human subjects. *Physiol. Meas.* 20(3):219– 240, 1999. https://doi.org/10.1088/0967-3334/20/3/301.
- Phillips, M. H., M. Kessler, F. Y. Chuang, K. A. Frankel, J. T. Lyman, J. I. Fabrikant, and R. P. Levy. Image correlation of MRI and CT in treatment planning for radiosurgery of intracranial vascular malformations. *Int. J. Radiat. Oncol. Biol. Phys.* 20(4):881–889, 1991. https://doi.org/10.1016/0360-3016(91)90036-4.
- Werba, N., J. Ludwig, C. Weiss, F. Struebing, S. Schoenberg, and M. Sadick. Extracranial arteriovenous malformations: a 10-year experience at a German vascular anomaly center and evaluation of diagnostic imaging for endovascular therapy assessment. *Front. Med.* (*Lausanne*). 11:1473685, 2024. https://doi.org/10.3389/ fmed.2024.1473685.
- Schubert, T., Y. Wu, K. M. Johnson, O. Wieben, J. Maksimovic, C. Mistretta, and P. Turski. Time-of-arrival parametric maps and virtual bolus images derived from contrast-enhanced timeresolved radial magnetic resonance angiography improve the display of brain arteriovenous malformation vascular anatomy. *Investig. Radiol.* 51(11):706–713, 2016. https://doi.org/10.1097/ RLI.000000000000000288.

- Bond, J. E., V. Smith, N. J. Yue, and J. P. Knisely. Comparison of an image registration technique based on normalized mutual information with a standard method utilising implanted markers in the staged radiosurgical treatment of large arteriovenous malformations. *Int. J. Radiat. Oncol. Biol. Phys.* 57(4):1150–1158, 2003. https://doi.org/10.1016/s0360-3016(03)01568-2.
- Sadick, M., D. Overhoff, B. Baessler, N. von Spangenberg, L. Krebs, and W. A. Wohlgemuth. Peripheral vascular anomalies—essentials in periinterventional imaging. *Rofo*. 192(2):150–162, 2020. https://doi.org/10.1055/a-0998-4300. (English, Epub 2019 Oct 17)
- Dunham, G. M., C. R. Ingraham, J. H. Maki, and S. S. Vaidya. Finding the nidus: detection and workup of non-central nervous system arteriovenous malformations. *Radiographics*. 36(3):891– 903, 2016. https://doi.org/10.1148/rg.2016150177.
- Schmidt, V. F., M. Masthoff, M. Czihal, B. Cucuruz, B. Häberle, R. Brill, W. A. Wohlgemuth, and M. Wildgruber. Imaging of peripheral vascular malformations—current concepts and future perspectives. *Mol. Cell. Pediatr.* 8(1):19, 2021. https://doi.org/10. 1186/s40348-021-00132-w.
- Calastra, C. G., E. Kleban, F. N. Helfenstein, F. Haupt, A. A. Peters, A. Huber, H. von Tengg-Kobligk, and B. Jung. Dynamic contrast-enhanced MRA of the aorta using a Golden-angle RAdial Sparse Parallel (GRASP) sequence: comparison with conventional time-resolved Cartesian MRA (TWIST). *Int. J. Cardiovasc. Imaging*. 2024. https://doi.org/10.1007/s10554-024-03259-9.
- Hadizadeh, D. R., V. C. Keil, G. Jost, H. Pietsch, M. Weibrecht, C. Marx, and W. Willinek. Contrast media in time-resolved MRA at 3 T: a systematic quantitative and qualitative analysis of concentration and dose effects on image parameters in minipigs. *Rofo*. 190(8):747–757, 2018. https://doi.org/10.1055/a-0631-4707. (English, Epub 2018 July 25)
- Goyen, M., T. C. Lauenstein, C. U. Herborn, J. F. Debatin, S. Bosk, and S. G. Ruehm. 0.5 M Gd chelate (Magnevist) versus 1.0 M Gd chelate (Gadovist): dose-independent effect on image quality of pelvic three-dimensional MR-angiography. *J. Magn. Reson. Imaging*. 14(5):602–607, 2001. https://doi.org/10.1002/jmri.1225.
- Frayne, R., R. A. Omary, O. Unal, and C. M. Strother. Determination of optimal injection parameters for intraarterial gadolinium-enhanced MR angiography. *J. Vasc. Interv. Radiol.* 11(10):1277–1284, 2000. https://doi.org/10.1016/s1051-0443(07)61301-3.
- Boos, M., K. Scheffler, R. Haselhorst, E. Reese, J. Fröhlich, and G. M. Bongartz. Arterial first pass gadolinium-CM dynamics as a function of several intravenous saline flush and Gd volumes. *J. Magn. Reson. Imaging*. 13(4):568–576, 2001. https://doi.org/10. 1002/jmri.1080.
- 61. Reiser, U. J. Study of bolus geometry after intravenous contrast medium injection: dynamic and quantitative measurements (Chronogram) using an X-ray CT device. *J. Comput. Assist. Tomogr.* 8:251–262, 1984.

**Publisher's Note** Springer Nature remains neutral with regard to jurisdictional claims in published maps and institutional affiliations.



#### **Authors and Affiliations**

Camilla Giulia Calastra 1 • Marika Bono 2 · Aloma Blanch Granada 3 • Aleksandra Tuleja 4 • Sarah Maike Bernhard 4 • Vanessa Diaz-Zuccarini 3,5 • Stavroula Balabani 3,5 • Dominik Obrist 4 • Hendrik von Tengg-Kobligk 1,6,7 • Bernd Jung 1,6 •

☐ Camilla Giulia Calastra camilla.calastra@yahoo.com

Marika Bono m.marikabono@gmail.com

Aloma Blanch Granada aloma.granada.20@ucl.ac.uk

Aleksandra Tuleja aleksandra.tuleja@insel.ch

Sarah Maike Bernhard sarah.bernhard@insel.ch

Vanessa Diaz-Zuccarini v.diaz@ucl.ac.uk

Stavroula Balabani s.balabani@ucl.ac.uk

Dominik Obrist dominik.obrist@unibe.ch

Hendrik von Tengg-Kobligk Hendrik.vontengg@insel.ch

Bernd Jung bernd.jung@insel.ch

- Department of Diagnostic, Interventional and Pediatric Radiology (DIPR), Inselspital, Bern University Hospital, University of Bern, Bern, Switzerland
- ARTORG Center for Biomedical Engineering Research, University of Bern, Bern, Switzerland
- Department of Mechanical Engineering, University College London, Torrington Place, London WC1E 7JE, UK
- Division of Angiology, Swiss Cardiovascular Center, Inselspital, Bern University Hospital, University of Bern, Bern, Switzerland
- Wellcome/EPSRC Centre for Interventional and Surgical Sciences (WEISS), Department of Medical Physics and Biomedical Engineering, University College London, 43-45 Foley Street, London W1W 7TS, UK
- Translational Imaging Center (TIC), Swiss Institute for Translational and Entrepreneurial Medicine, Bern, Switzerland
- Experimental Radiology, Department of BioMedical Research, University of Bern, Bern, Switzerland

